19. Decharms, R. C. & Merzenich, M. M. Primary cortical representation of sounds by the coordination of action potential timing. *Nature* **381,** 610–613 (1996).
20. Roy, S. & Calloway, K. D. Synchronization of Local Neural Networks in the Somatosensory Cortex. A Comparison of Stationary and Moving Stimuli. *J. Neurophysiol.* **81,** 999–1013 (1999).
21. Crick, F. & Koch, C. Towards a neurobiological theory of consciousness. *Sem. Neurosci.* **2,** 263–275 (1990).
22. DiCarlo, J. J., Lane, J. W., Hsiao, S. S. & Johnson, K. O. Marking microelectrode penetrations with fluorescent dyes. *J. Neurosci. Methods* **54,** 75–81 (1996).
23. Brody, C. D. Slow covariations in neuronal resting potentials can lead to artefactually fast cross-correlations in their spike trains. *J. Neurophysiol.* **80,** 3345–3351 (1998).
24. Efron, B. & Tibshirani, R. J. *An Introduction to the Bootstrap* (Chapman and Hall, New York, 1993).
25. Roy, A., Steinmetz, P. N., Johnson, K. O. & Niebur, E. Model-free detection of synchrony in neuronal spike trains, with an application to primate somatosensory cortex. *Neurocomputing* (in the press).

Acknowledgements

This work was supported by the NIH, the NSF and the Alfred P. Sloan Foundation. We thank J. DiCarlo, M. Usher and S. Yantis for discussions and J. Lane for technical support.

Correspondence and requests for materials should be addressed to E.N. (e-mail: niebur@jhu.edu).

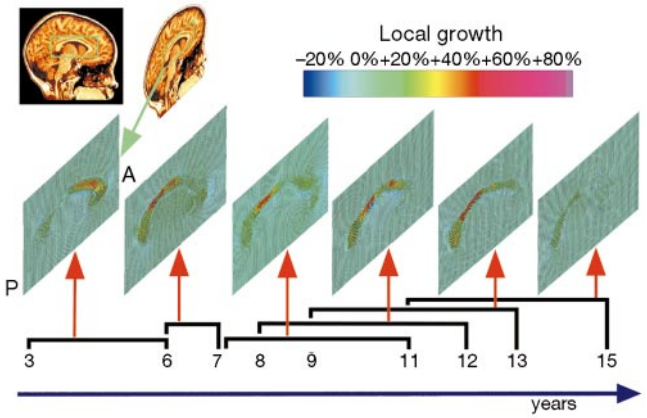

Figure 1 Growth patterns in the developing human brain detected at ages 3–15 years. A rostro-caudal wave of peak growth rates is detected in young normal subjects scanned repeatedly across time spans of up to four years. Between ages 3 and 6 years, peak growth rates (red colours; 60–80% locally) were detected in the frontal circuits of the corpus callosum, which sustain mental vigilance and regulate the planning of new actions. Older children displayed fastest growth at the callosal isthmus, which innervates temporo-parietal systems supporting spatial association and language function. Between ages 11–15 years, growth rates still peak at the isthmus, but are attenuated.

Growth patterns in the developing brain detected by using continuum mechanical tensor maps

Paul M. Thompson*, Jay N. Giedd†, Roger P. Woods*, David MacDonald‡, Alan C. Evans‡ & Arthur W. Toga*

**Laboratory of Neuro Imaging, Department of Neurology, Division of Brain Mapping, UCLA School of Medicine, 710 Westwood Plaza, Los Angeles, California 90095-1769, USA*
† *Child Psychiatry Branch, National Institute of Mental Health, NIH, 10 Center Drive, MSC 1600, Bethesda 20982-1600, Maryland, USA*
‡ *Montreal Neurological Institute, McGill University, 3801 University Street, Montreal, Québec, Canada H3A 2B4*

The dynamic nature of growth and degenerative disease processes requires the design of sensitive strategies to detect, track and quantify structural change in the brain in its full spatial and temporal complexity[1]. Although volumes of brain substructures are known to change during development[2], detailed maps of these dynamic growth processes have been unavailable. Here we report the creation of spatially complex, four-dimensional quantitative maps of growth patterns in the developing human brain, detected using a tensor mapping strategy with greater spatial detail and sensitivity than previously obtainable. By repeatedly scanning children (aged 3–15 years) across time spans of up to four years, a rostro-caudal wave of growth was detected at the corpus callosum, a fibre system that relays information between brain hemispheres. Peak growth rates, in fibres innervating association and language cortices, were attenuated after puberty, and contrasted sharply with a severe, spatially localized loss of subcortical grey matter. Conversely, at ages 3–6 years, the fastest growth rates occurred in frontal networks that regulate the planning of new actions. Local rates, profiles, and principal directions of growth were visualized in each individual child.

Time series of high-resolution three-dimensional magnetic resonance imaging (MRI) scans were acquired across large time spans from young normal subjects (aged 3–6, 6–7, 7–11, 8–12, 9–13 and 11–15 years) at intervals ranging from two weeks to four years. Growth patterns were recovered by computing a three-dimensional elastic deformation field, which reconfigures the anatomy at the earlier time point into the shape of the anatomy of the later scan.

Maps of local growth rates (Figs 1–4) revealed the complexity and regional heterogeneity of the tissue growth, pruning and maturation processes of late brain development. In subjects aged 6–15 years, the

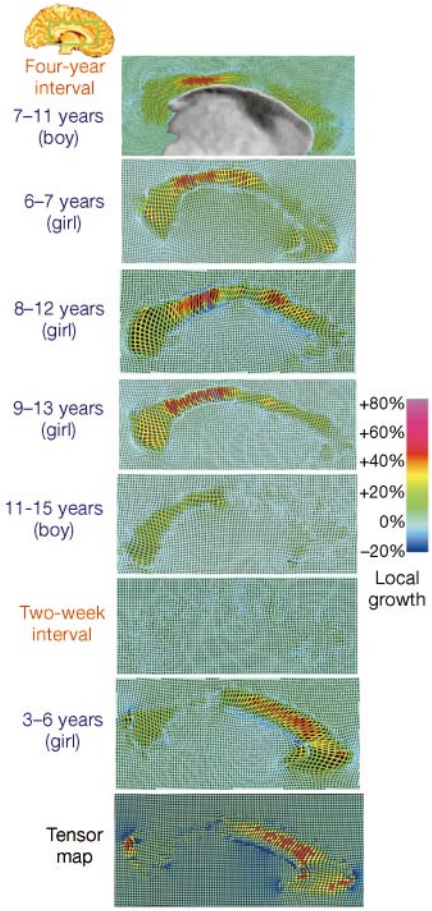

Figure 2 Mapping dynamic patterns of brain development: four-dimensional growth maps. Strikingly similar growth rates were detected in the corpus callosum of five young normal subjects scanned repeatedly aged 6–13 years. Peak values throughout the posterior midbody (red colours) were attenuated after puberty (11–15 years). By contrast, near-zero maps of change were observed between scans acquired over a two-week interval. Between ages 3–6 years, extreme growth rates were found in the anterior interhemispheric fibre systems that transfer information to sustain mental vigilance and organize new actions. Tensor maps identify the principal directions of growth rates, revealing an outward radial tissue expansion in frontal regions.

highest growth rates were consistently attained in temporo-parietal systems which are functionally specialized for language, and for understanding spatial relations (Fig. 2). In contrast to the near-zero maps of change recovered at short time intervals ('Two-week interval' in Fig. 2), growth maps spanning large time intervals showed complex and heterogeneous patterns of change. Between ages 7 and 11 years (Fig. 2), comparative stability of the splenial and rostral fibre systems of the corpus callosum contrasted sharply with rapid focal growth at the callosal isthmus (up to 80%). Although global measurements indicated an overall 22.4% increase in mid-sagittal callosal area during the four-year time span (from 527.6 mm^2 to 645.6 mm^2), these global values disguise the complexity of local growth patterns. Local growth is as high as 80% (Fig. 2), a feature which may not be apparent with conventional volumetric descriptors.

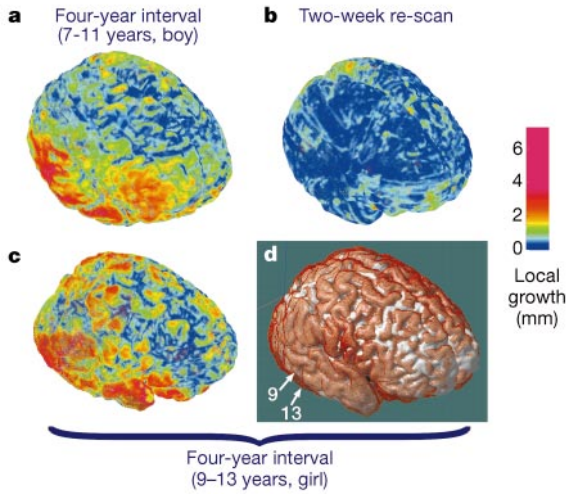

Figure 3 Patterns of cerebral growth. **a**, In a subject scanned at age 7 years and again exactly four years later at age 11 years, dramatic growth is found in temporo-parietal regions (red colours). **b**, All brain regions are stable in a control experiment (blue colours) analysing scans acquired two weeks apart. **c**, Between ages 9–13 years, growth is also most pronounced in temporo-parietal regions. **d**, This was confirmed by digitally overlaying models of the cerebral cortex at each time point (arrows 9 and 13). Growth at the callosal isthmus in subjects aged 7–11 and 9–13 years (Fig. 2) is therefore accompanied by diffuse growth in its (temporo-parietal) lobar projection zones.

Although some individual variation was expected, this focus of extreme growth at the callosal isthmus was detected consistently in all subjects tracked between 6 and 15 years (Fig. 2), suggesting that cortico-cortical networks supporting rapid associative relay and language functions may myelinate more extensively[3] and over longer periods than rostral fibre systems. In a girl scanned twice exactly one year apart at ages 6 and 7 years, extreme growth (up to 85%) at the callosal isthmus contrasted with a comparatively quiescent region in the more rostral systems that innervate frontal and pre-frontal cortices. When a four-year growth map was generated for a slightly older child (11–15 years, Fig. 2), growth rates were correspondingly reduced in every region. Nonetheless, growth patterns at the isthmus and splenium (commonly defined as the posterior fifth of the callosum) were still more rapid (20–25% locally) than in the more anterior rostrum and genu (near-zero change). In an analysis of grey matter at the cortex[4], we recently observed a localized grey matter loss in frontal cortex that persists in normal subjects throughout adolescence even into adulthood. The gradual quiescence of growth at the rostral callosum around puberty may therefore be a precursor to a prolonged regressive process of grey matter loss through adolescence into adulthood in the frontal circuits it innervates.

Several near-zero maps of change were recovered at short time intervals. Figure 2 shows a typical map from a subject scanned at age 8 years, exactly four years later at age 12 years, and again two weeks later. Negligible change at short time intervals ('Two-week interval' in Fig. 2) contrasted with a highly heterogeneous map of growth across the four-year time span. Growth rates again achieved their highest rates in the associative and linguistic networks that cross at the callosal isthmus.

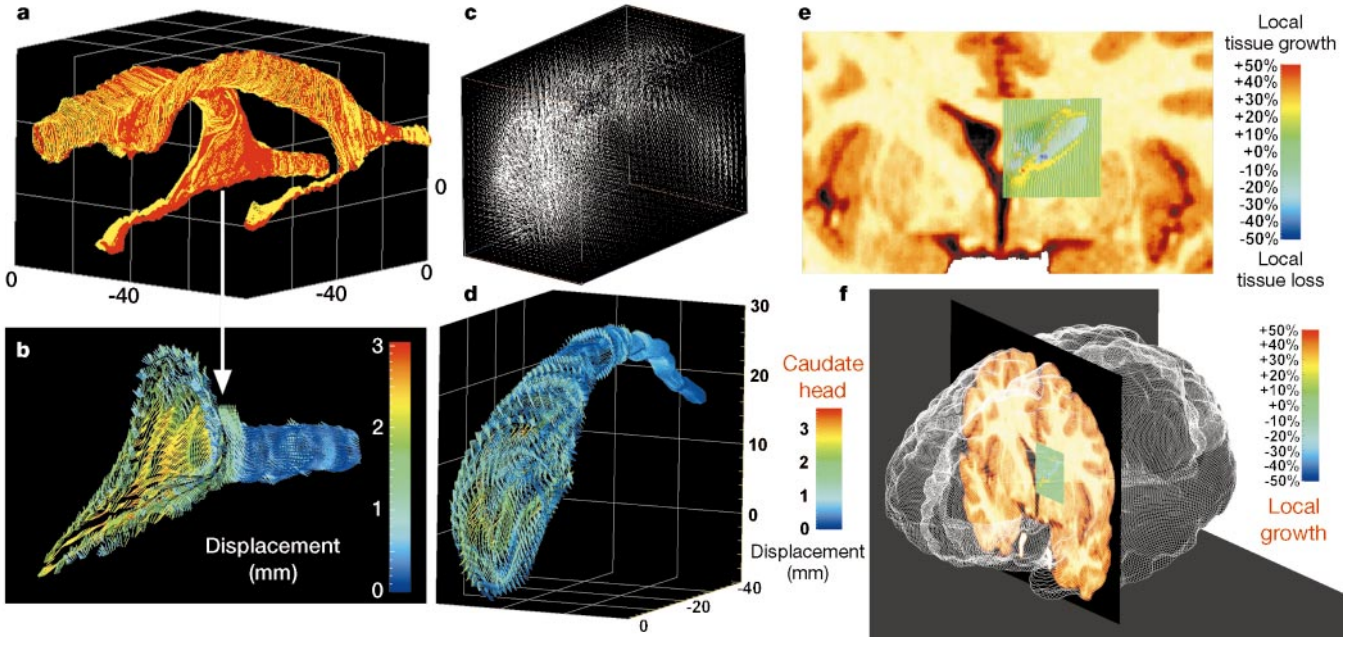

Figure 4 Detecting three-dimensional patterns of deep nuclear tissue loss. **a**, **b**, Tensor maps distinguish local growth or brain tissue loss from global displacements (**b**) of the adjacent ventricular anatomy, modelled here (**a**) at ages 7 years (red) and 11 years (yellow). **c**, **d**, Between ages 7 and 11 years, three-dimensional displacement vector maps show the deformation required to reconfigure earlier models of the caudate head into their later shape. The caudate tail is stable (blue colours, **d**). **e**, **f**, Local growth (**e**) and anatomical displacement (**d**) of the caudate head are independently recovered, with 50% tissue loss detected locally (**e**, **f**), adjacent to a region of 20–30% growth throughout the internal capsule.

A subject scanned at ages 3 and 6 years exhibited a focus of peak growth rates (60–80% locally) throughout the anterior corpus callosum, in frontal circuits that help to sustain a vigilant mental state and regulate the organization and planning of new actions. The extremely rapid rates of local growth are consistent with metabolic studies using positron emission tomography[5], which show an extraordinary doubling of the rates of glucose metabolism in the frontal cortex between ages 2 and 4 years, with frontal metabolic rates remaining at 199% of their adult values throughout the age range of 3–8 years. Between ages 3 and 6 years, when language function and associative thinking are not yet fully developed, growth rates at the isthmus were more quiescent (Fig. 2; 0–20% growth). Later growth foci in the isthmus, found consistently in all subjects aged 6–15 years, may reflect fine tuning of language functions known to occur late in childhood.

Regressive processes (tissue loss) were also detected at the same time as rapid growth. In the 7–11 and 9–13 year old subjects (Fig. 3), maps of lobar growth revealed pronounced (2–6 mm) temporo-parietal and pre-frontal enlargement. Somatosensory, motor and occipital brain regions were comparatively stable, with near-zero change in all brain regions at short time intervals (Fig. 3b). Up to 50% loss of tissue volume was detected at the caudate head (Fig. 4e and f). This tissue loss was highly localized, and contrasted with a 20–30% growth of the adjacent internal capsule (for which a separate surface model was made) and a 5–10% dilation of the superior ventricular horn (Fig. 4a). Gross volumetric measures confirmed an overall 60 mm^3 tissue loss at the caudate head, although these global measures disguise the regional complexity of the change. This example helps illustrate how tensor maps distinguish local growth patterns (Fig. 4e) from bulk shifts, such as global displacements of the adjacent cerebral ventricles (Fig. 4a and b). Three-dimensional vector displacement maps (Fig. 4b and d) emphasize that both global and local displacements are required to match modelled anatomical elements across time. The three-dimensional deformation field, however, encodes the patterns of local anatomical dilation and contraction, and its values are unaffected by global displacements. Maps of local three-dimensional growth are therefore not critically dependent on how well scans are initially aligned, and can define growth at arbitrary three-dimensional points in the local anatomy (Fig. 4e). Figure 4f indicates the anatomical context and regional complexity of these growth and regressive processes. The foci of tissue loss corroborate the hypothesis that pruning processes occur during this developmental stage[2], suggesting that these processes can be tracked in an individual child.

We detected striking, spatially complex patterns of growth and tissue loss in the developing human brain. A rostro-caudal wave of peak growth rates (Fig. 1) was identified in the corpus callosum. Fibre systems that mediate language function and associative thinking grew more rapidly than surrounding regions across time spans before and during puberty (6–13 years), with growth attenuated shortly afterwards (11–15 years). This temporal pattern coincides with the ending of a well-known critical period for learning language, consistently noted in studies of second-language acquisition, including sign language, and in isolated children not exposed to language during early development[6]. The ability to learn new languages declines rapidly after the age of 12 years, as does the ability to recover language function if linguistic areas in one brain hemisphere are surgically resected. Peak growth rates in linguistic callosal regions, as well as their attenuation around puberty, may reflect the conclusion of the critical period for learning language and for accelerating signal transduction in networks that support both associative reasoning and language function. We recently found that the same temporo-parietal fibre system, crossing at the callosal isthmus, degenerates fastest in early Alzheimer's disease[7], when progressive neuronal loss and perfusion deficits begin to occur in temporo-parietal association cortices and their commissural projection systems. The sensitivity of the approach may therefore offer advantages in tracking fine-scale effects of therapeutic interventions in dementia and oncology, mapping the local complexities of disease processes using dynamic rather than static criteria. □

Methods

Magnetic resonance imaging and pre-processing

Three-dimensional ($256^2 \times 124 \times 0.97\ mm \times 0.97\ mm \times 1.5\ mm$ resolution) T_1-weighted fast SPGR (spoiled GRASS (gradient-recalled acquisition in the steady state)) MRI volumes were acquired from young normal subjects (mean age 8.6 ± 3.1 years) at intervals ranging from two weeks to four years. For each scan pair, a radio-frequency bias field correction algorithm[8] was applied to both scans to eliminate intensity drifts caused by scanner field inhomogeneity. The initial scan was then rigidly registered to the target using automated image registration software[9] and resampled using chirp-Z (in-plane) and linear (out-of-plane) interpolation. Registered scans were histogram-matched (that is, their intensity distributions were equalized) and a preliminary map of differences in MRI signal intensities between the two scans was constructed[1,10]. Tensor models of structural change were then used to calculate rates of tissue dilation, contraction and shearing, mapping local patterns of change in three dimensions.

Image analysis

A high-resolution surface model of the cortex was automatically extracted[11] from each scan pair, and three-dimensional digital anatomical models, based on parametric surface meshes[12,13], were generated to represent a comprehensive set of deep sulcal, callosal, caudate and ventricular surfaces at each time point[14]. Surface models based on manually digitized data were averaged across multiple trials ($N = 6$) to minimize error[15]. These model surfaces provided anatomic constraints for an elastic image registration algorithm[12,14]. For each subject, this algorithm calculated a three-dimensional elastic deformation vector field, with $384^2 \times 256 \times 3 \approx 0.1$ billion degrees of freedom, reconfiguring the anatomy at the earlier time point into the shape of the anatomy of the later scan. Surface deformations were used to derive a volumetric deformation field from which local measures of three-dimensional tissue dilation or contraction were quantified. Landmark points, surfaces, and curved anatomic interfaces were matched up in the pair of three-dimensional image sets, and the biological validity of the resulting anatomical transformation was guaranteed by forcing a large system of anatomical surface boundaries to match exactly. These included multiple structural, functional, and tissue type boundaries in three dimensions, including the callosum, caudate, cortex and ventricles. The deformation field driving the earlier onto the later anatomy was extended to the full volume using a continuum-mechanical model based on the Cauchy–Navier operator of linear elasticity[14,16–18]. The resulting system of 0.1 billion second-order elliptic partial differential equations was solved by successive over-relaxation methods, with multi-grid acceleration[12,14], on a standard radiologic workstation. Potential artefactual differences due to differences in how surfaces were parametrized in each scan were compensated for, using a field of Christoffel symbols to modify the surface differential operators during the anatomical transformation[14].

Tensor map computation

From this transformation, local rates of tissue dilation, contraction and shearing were calculated. Deformation processes recovered by the image-matching algorithm were analysed mathematically with vector field operators[14] to produce a variety of tensor maps. These maps reflect the magnitude and principal directions of tissue dilation or contraction, and the local rates, divergence and gradients of the growth processes detected in the dynamically changing brain.

Received 27 August 1999; accepted 21 January 2000.

1. Fox, N. C., Freeborough, P. A. & Rossor, M. N. Visualisation and quantification of rates of atrophy in Alzheimer's disease. *Lancet* **348,** 94–97 (1996).
2. Giedd, J. N. *et al.* Quantitative magnetic resonance imaging of human brain development: ages 4–18. *Cereb. Cortex* **6,** 551–560 (1996).
3. Yakovlev, P. I. & Lecours, A. R. in *Regional Development of the Brain in Early Life* (ed. Minkowski, A.) 3–70 (Davis, Philadelphia, 1967).
4. Sowell, E. R., Thompson, P. M., Holmes, C. J., Jernigan, T. L. & Toga, A. W. *In vivo* evidence for post-adolescent brain maturation frontal and striatal regions. *Nature Neurosci.* **2,** 859–861 (1999).
5. Chugani, H. T., Phelps, M. E. & Mazziotta, J. C. Positron emission tomography study of human brain functional development. *Ann. Neurol.* **22,** 487–497 (1987).
6. Grimshaw, G. M., Adelstein, A., Bryden, M. P. & MacKinnon, G. E. First-language acquisition in adolescence: evidence for a critical period for verbal language development. *Brain Lang.* **63,** 237–255 (1998).
7. Thompson, P. M. *et al.* Cortical variability and asymmetry in normal aging and Alzheimer's disease. *Cereb. Cortex* **8,** 492–509 (1998).
8. Zijdenbos, A. P. & Dawant, B. M. Brain segmentation and white matter lesion detection in MR images. *Crit. Rev. Biomed. Eng.* **22,** 401–465 (1994).
9. Woods, R. P., Cherry, S. R. & Mazziotta, J. C. Rapid automated algorithm for aligning and reslicing PET images. *J. Comp. Assist. Tomogr.* **16,** 620–633 (1992).
10. Freeborough, P. A., Woods, R. P. & Fox, N. C. Accurate registration of serial 3D MR brain images and its application to visualizing change in neurodegenerative disorders. *J. Comp. Assist. Tomogr.* **20,** 1012–1022 (1996).
11. MacDonald, D., Avis, D. & Evans, A. C. in *Proc. SPIE Conf. Visualization in Biomedical Computing* (ed. Robb, R. A.) **2359,** 160–169 (1994).

12. Thompson, P. M. & Toga, A. W. A surface-based technique for warping 3-dimensional images of the brain. *IEEE Trans. Med. Imag.* **15,** 471–489 (1996).
13. Thompson, P. M. & Toga, A. W. Detection, visualization and animation of abnormal anatomic structure with a deformable probabilistic brain atlas based on random vector field transformations. *Med. Image Anal.* **1,** 271–294 (1997).
14. Thompson, P. M. & Toga, A. W. in *Brain Warping* (ed. Toga, A. W.) 311–336 (Academic, San Diego, 1998).
15. Thompson, P. M., Schwartz, C., Lin, R. T., Khan, A. A. & Toga, A. W. 3D statistical analysis of sulcal variability in the human brain. *J. Neurosci.* **16,** 4261–4274 (1996).
16. Thompson, P. M. *et al.* Detection and mapping of abnormal brain structure with a probabilistic atlas of cortical surfaces. *J. Comp. Assist. Tomogr.* **21,** 567–581 (1997).
17. Davatzikos, C. Spatial normalization of 3D brain images using deformable models. *J. Comp. Assist. Tomogr.* **20,** 656–665 (1996).
18. Miller, M. I. & Grenander, U. Computational anatomy: an emerging discipline. *Q. Appl. Math.* **56,** 617–694 (1998).

Correspondence and requests for materials should be addressed to P.M.T. (e-mail: thompson@loni.ucla.edu).

Acknowledgements

We thank E. Sowell, M. Mega and J. Mazziotta for their advice and support. P.M.T. was supported by the Howard Hughes Medical Institute, the US Information Agency, and the US–UK Fulbright Commission. Additional research support was provided by a Human Brain Project grant to the International Consortium for Brain Mapping, funded jointly by NIMH and NIDA, by National Institutes of Health intramural funding (J.N.G.), and by the National Library of Medicine, National Science Foundation, and the NCRR.

A clonogenic common myeloid progenitor that gives rise to all myeloid lineages

Koichi Akashi*†, David Traver*, Toshihiro Miyamoto & Irving L. Weissman

Departments of Pathology and Developmental Biology, Stanford University School of Medicine, Stanford, California 94305, USA
** These authors contributed equally to this work*

Haematopoietic stem cells give rise to progeny that progressively lose self-renewal capacity and become restricted to one lineage[1,2]. The points at which haematopoietic stem cell-derived progenitors commit to each of the various lineages remain mostly unknown. We have identified a clonogenic common lymphoid progenitor that can differentiate into T, B and natural killer cells but not myeloid cells[3]. Here we report the prospective identification, purification and characterization, using cell-surface markers and flow cytometry, of a complementary clonogenic common myeloid progenitor that gives rise to all myeloid lineages. Common myeloid progenitors give rise to either megakaryocyte/erythrocyte or granulocyte/macrophage progenitors. Purified progenitors were used to provide a first-pass expression profile of various haematopoiesis-related genes. We propose that the common lymphoid progenitor and common myeloid progenitor populations reflect the earliest branch points between the lymphoid and myeloid lineages, and that the commitment of common myeloid progenitors to either the megakaryocyte/erythrocyte or the granulocyte/macrophage lineages are mutually exclusive events.

The existence of clonal common lymphoid progenitors (CLPs)[3] suggests that complementary progenitors common to all myeloid cells may also exist. Because the expression of the interleukin-7 receptor α-chain (IL-7Rα) marks the CLPs and other downstream lymphoid progenitors[3,4], we searched the IL-7Rα$^-$ fraction of murine bone marrow for primitive myeloid progenitor populations.

In steady-state mouse bone marrow, myeloerythroid colony-forming unit (CFU) activity was found almost exclusively in the IL-7Rα$^-$Lin$^-$c-Kit$^+$fraction (data not shown). Within this population, Sca-1$^+$ cells are highly enriched for haematopoietic stem cells (HSCs)[3,5–7]. To remove HSCs, Sca-1$^+$ cells were excluded. The IL-7Rα$^-$Lin$^-$c-Kit$^+$Sca-1$^-$ fraction was further divided into three subpopulations according to the expression profiles of the Fcγ receptor-II/III (FcγR), an important marker for myelomonocytic cells and a progenitor marker in fetal liver haematopoiesis[8], and CD34, which marks a fraction of haematopoietic stem cells and progenitors[6]: the FcγR^{lo}CD34$^+$, FcγR^{lo}CD34$^-$, and FcγR^{hi}CD34$^+$ populations (Fig. 1a).

Each of the above populations were cleanly isolatable (Fig. 1b) and gave rise to distinct colony types in methylcellulose CFU assays (Figs 1c and 2). In the presence of steel factor (Slf), Flt-3 ligand (FL), IL-11, IL-3, granulocyte/macrophage-colony stimulating factor (GM-CSF), erythropoietin (Epo) and thrombopoietin (Tpo), ~80% of single multipotent HSCs randomly committed to myeloid lineages[9], giving rise to various types of myeloid colonies including CFU-Mix[10], burst-forming units-erythroid (BFU-E),

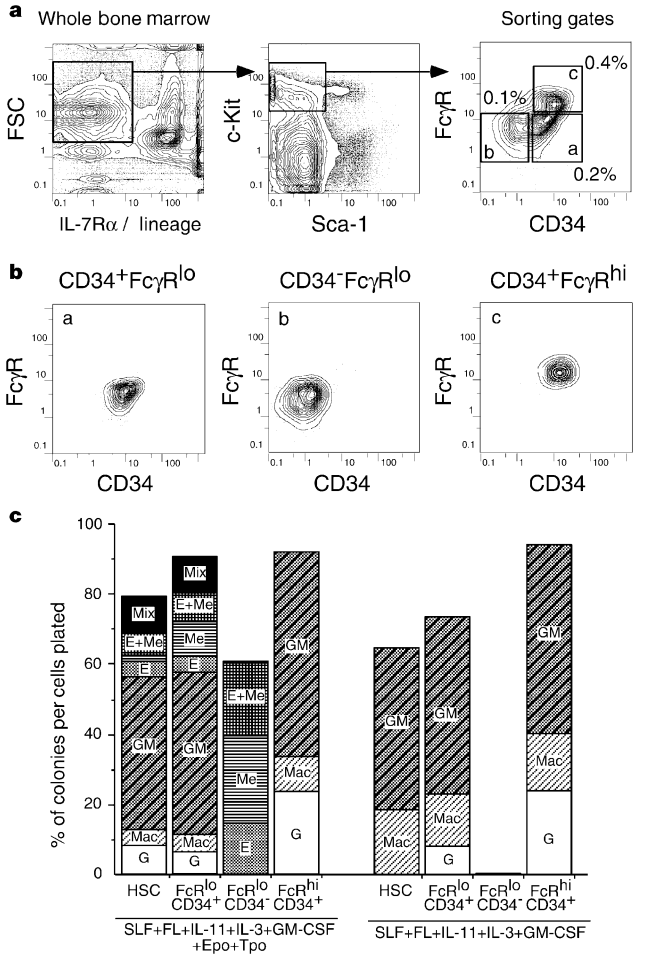

Figure 1 Identification of myeloid progenitors in mouse bone marrow. **a**, The IL-7Rα$^-$Lin$^-$Sca-1$^-$c-Kit$^+$ fraction was subdivided into FcγR^{lo}CD34$^+$, FcγR^{lo}CD34$^-$, and FcγR^{hi}CD34$^+$ populations (a, b, c respectively as indicated in the right-hand panel). Percentages of each population relative to whole bone marrow are shown next to each sort gate. **b**, Re-analysis of the sorted FcγR^{lo}CD34$^+$, FcγR^{lo}CD34$^-$ and FcγR^{hi}CD34$^+$ populations. **c**, Clonogenic myeloid colony formation in methylcellulose. From each sorted progenitor population, 288 wells receiving a single cell each were scored. FcγR^{lo}CD34$^+$cells and HSCs formed various myeloid colonies including CFU-Mix, whereas the FcγR^{lo}CD34$^-$ and FcγR^{hi}CD34$^+$ populations gave rise only to MegE and GM colonies, respectively (left). Megakaryocyte/erythroid colony formation from the FcγR^{lo} fractions was dependent upon Epo and/or Tpo (right).

† Present address: Department of Cancer Immunology and AIDS, Dana-Farber Cancer Institute, 44 Binney Street, Boston, Massachusetts 02115, USA.